

THE MOLECULAR CLOUD S242: PHYSICAL ENVIRONMENT AND STAR FORMATION ACTIVITIES

L. K. DEWANGAN¹, T. BAUG², D. K. OJHA², P. JANARDHAN¹, R. DEVARAJ³, AND A. LUNA³

ABSTRACT

We present a multi-wavelength study to probe the star formation (SF) processes on a larger scale ($\sim 1^\circ.05 \times 0^\circ.56$) around the S242 site. The S242 molecular cloud is depicted in a velocity range from -3.25 to 4.55 km s⁻¹ and has spatially elongated appearance. Based on the virial analysis, the cloud is prone to gravitational collapse. The cloud harbors an elongated filamentary structure (EFS; length ~ 25 pc) evident in the *Herschel* column density map and the EFS has an observed mass per unit length of ~ 200 M_⊙ pc⁻¹ exceeding the critical value of ~ 16 M_⊙ pc⁻¹ (at T = 10 K). The EFS contains a chain of *Herschel* clumps (M_{clump} ~ 150 to 1020 M_⊙), revealing the evidence of fragmentation along its length. The most massive clumps are observed at both the EFS ends, while the S242 H II region is located at one EFS end. Based on the radio continuum maps at 1.28 and 1.4 GHz, the S242 H II region is ionized by a B0.5V–B0V type star and has a dynamical age of ~ 0.5 Myr. The photometric 1–5 μm data analysis of point-like sources traces young stellar objects (YSOs) toward the EFS and the clusters of YSOs are exclusively found at both the EFS ends, revealing the SF activities. Considering the spatial presence of massive clumps and YSO clusters at both the EFS ends, the observed results are consistent with the prediction of a SF scenario of the end-dominated collapse driven by the higher accelerations of gas.

Subject headings: dust, extinction – HII regions – ISM: clouds – ISM: individual objects (Sh 2-242) – stars: formation – stars: pre-main sequence

1. INTRODUCTION

The *Herschel* continuum observations demonstrated clearly that the filaments are common features seen in the star-forming regions (e.g. André et al. 2010). The dust continuum maps have been utilized as a very useful tool to investigate the filaments and to infer the underlying structure(s) within the filaments. These filaments are observed at various scales and often contain the star-forming clumps and cores along their lengths (e.g. Schneider et al. 2012; Ragan et al. 2014; Contreras et al. 2016; Li et al. 2016, and references therein). However, the physical mechanisms concerning to their formation and their link to the star formation processes are not well understood. The role of filaments in the formation of dense massive star-forming clumps and clusters is also unknown (e.g. Myers 2009; Schneider et al. 2012; Nakamura et al. 2014; Tan et al. 2014; André et al. 2016; Kainulainen et al. 2016). In star-forming regions, the knowledge of physical conditions, kinematics of the molecular gas, and masses per unit length of filamentary features can help us to understand the ongoing physical processes.

The star-forming region, LBN 182.30+00.07 or Sh 2-242 (hereafter S242) is situated at a distance of 2.1 kpc (Blitz et al. 1982). The H II region linked with the S242 site (hereafter S242 H II region) is ionized by a star BD+26 980 of spectral type B0V (Hunter & Massey 1990). In the S242 H II region, Fich et al. (1990) reported the radial velocity of H α emission to be about -0.6 km s⁻¹. Using the CO line data, Blitz et al. (1982) estimated

the radial velocity of molecular gas to be 0.0 ± 0.5 km s⁻¹ toward S242. Kawamura et al. (1998) also studied the molecular gas content of molecular clouds in Gemini and Auriga including the S242 site using ¹³CO (1-0) emission (see S242 region around $l = 182^\circ.40$; $b = 0^\circ.27$ in Figures 1, 2, and 9j in Kawamura et al. 1998). They referred the molecular cloud associated with S242 as “182.4+00.3” cloud ($V_{lsr} \sim 0.7$ km s⁻¹; line width (ΔV) = 2.1 km s⁻¹) and estimated the mass of the cloud (M_{cloud}) to be ~ 7000 M_⊙ (radius ~ 7 pc; see source ID #73 in Table 1 in Kawamura et al. 1998). The cloud appears spatially elongated in the ¹³CO (1-0) map (see Figures 1 and 9j in Kawamura et al. 1998). However, the identification of filaments and their role in star formation processes are yet to be probed within the molecular cloud 182.4+00.3/S242. Snell et al. (1990) investigated a CO outflow toward IRAS 05490+2658 and found that this IRAS source is located $\sim 5'$ east of the S242 H II region. Beuther et al. (2002) investigated two 1.2 mm peaks toward IRAS 05490+2658 with the IRAM 30-m telescope (spatial resolution $\sim 11''$). The H₂ emission at 2.12 μm is also traced near the IRAS 05490+2658 (see Figure A9 in Varricatt et al. 2010) and they also mentioned the presence of two clusters of infrared excess sources near the IRAS 05490+2658. Together, these previous studies indicate that the S242 is an active site of star formation and also contains a massive star. However, the impact of the massive star in its vicinity is yet to be examined in this star-forming site. On a larger scale, the physical conditions around the S242 site are yet to be investigated. In this paper, to investigate the ongoing physical mechanisms in and around the S242 site, we carry out a detailed multi-wavelength study of observations from optical, near-infrared (NIR), mid-infrared (MIR), far-infrared (FIR), sub-millimeter (sub-mm), millimeter (mm) to centimeter (cm) wavelengths, including the Gi-

lokeshd@prl.res.in

¹ Physical Research Laboratory, Navrangpura, Ahmedabad - 380 009, India.² Department of Astronomy and Astrophysics, Tata Institute of Fundamental Research, Homi Bhabha Road, Mumbai 400 005, India.³ Instituto Nacional de Astrofísica, Óptica y Electrónica, Luis Enrique Erro # 1, Tonantzintla, Puebla, México C.P. 72840.

ant Metre-wave Radio Telescope (GMRT) radio continuum map at 1.28 GHz and United Kingdom Infra-Red Telescope (UKIRT) Infrared Deep Sky Survey (UKIDSS) NIR data.

In Section 2, we give the description of the multi-band data-sets utilized in the present work. In Section 3, the results concerning the physical environment and point-like sources are summarized. The possible star formation processes are discussed in Section 4. Finally, the main results are summarized and concluded in Section 5.

2. DATA AND ANALYSIS

In this work, we have selected a region of $\sim 1^\circ.05 \times 0^\circ.56$ (~ 38.5 pc \times 20.5 pc at a distance of 2.1 kpc) (central coordinates: $l = 182^\circ.217$; $b = 0^\circ.239$) around the S242 site. The target area is selected in such a way that it contains the previously known molecular cloud, “182.4+00.3”. In the following, we provide a brief description of the adopted multi-wavelength data-sets.

2.1. $H\alpha$ Image

We retrieved narrow-band $H\alpha$ image at $0.6563 \mu\text{m}$ from the Isaac Newton Telescope (INT) Photometric $H\alpha$ Survey of the Northern Galactic Plane (IPHAS; Drew et al. 2005) survey database. The IPHAS imaging survey was carried out using the Wide-Field Camera (WFC) at the 2.5-m INT, located at La Palma. The WFC contains four $4\text{k} \times 2\text{k}$ CCDs, in an L-shape configuration. The pixel scale is $0''.33$ (see Drew et al. (2005) for more details).

2.2. NIR (1–5 μm) Data

We utilized the NIR photometric magnitudes of point-like sources extracted from the UKIDSS DR10PLUS Galactic Plane Survey (GPS; Lawrence et al. 2007) and the Two Micron All Sky Survey (2MASS; Skrutskie et al. 2006) (hereafter GPS-2MASS). The UKIDSS observations (resolution $\sim 0''.8$) were made with the WFCAM mounted on the UKIRT. The 2MASS photometric data were utilized to calibrate the UKIDSS fluxes. In this work, we extracted only a reliable NIR photometric catalog. More information about the selection procedures of the GPS photometry can be obtained in Dewangan et al. (2015). To obtain reliable 2MASS photometric data, we selected only those sources having photometric magnitude error of 0.1 or less in each band.

Warm-*Spitzer* IRAC 3.6 and $4.5 \mu\text{m}$ photometric images (resolution $\sim 2''$) and magnitudes of point sources are downloaded from the Glimpse360¹ (Whitney et al. 2011) survey. The photometric magnitudes were extracted from the Glimpse360 highly reliable catalog. To obtain further reliable Glimpse360 photometric data, we retrieved only those sources having photometric magnitude error of 0.2 or less in each band.

2.3. Mid-infrared (12–22 μm) Data

MIR images at $12 \mu\text{m}$ (spatial resolution $\sim 6''$) and $22 \mu\text{m}$ (spatial resolution $\sim 12''$) were obtained from the publicly available archival WISE² (Wright et al. 2010) database.

¹ <http://www.astro.wisc.edu/sirtf/glimpse360/>

² Wide Field Infrared Survey Explorer, which is a joint project of the University of California and the JPL, Caltech, funded by the NASA.

2.4. Far-infrared and Sub-millimeter Data

We utilized the *Herschel* Space Observatory data archives to obtain FIR and sub-mm continuum images. The processed level2_5 images at $70 \mu\text{m}$, $160 \mu\text{m}$, $250 \mu\text{m}$, $350 \mu\text{m}$, and $500 \mu\text{m}$ were downloaded using the *Herschel* Interactive Processing Environment (HIPE, Ott 2010). The beam sizes of the *Herschel* images at $70 \mu\text{m}$, $160 \mu\text{m}$, $250 \mu\text{m}$, $350 \mu\text{m}$, and $500 \mu\text{m}$ are $5''.8$, $12''$, $18''$, $25''$, and $37''$, respectively (Poglitsch et al. 2010; Griffin et al. 2010). In this work, *Herschel* temperature and column density maps are produced using the *Herschel* continuum images, following the methods described in Mallick et al. (2015). The *Herschel* temperature and column density maps are obtained from a pixel-by-pixel spectral energy distribution (SED) fit with a modified blackbody to the cold dust emission at *Herschel* 160–500 μm (also see Dewangan et al. 2015). The *Herschel* 70 μm data are not included in the analysis, because the 70 μm emission is dominated by the ultraviolet (UV) heated warm dust. Here we provide a brief step-by-step explanation of the procedures.

The *Herschel* 160 μm image is in unit of Jy pixel^{-1} , while the images at 250–500 μm are in units of surface brightness, MJy sr^{-1} . The plate scales of 160, 250, 350, and 500 μm images are $3''.2$, $6''$, $10''$, and $14'' \text{ pixel}^{-1}$, respectively. Prior to the SED fit, the 160–350 μm images were convolved to the lowest angular resolution of 500 μm image ($\sim 37''$) and were converted into the same flux unit (i.e. Jy pixel^{-1}). Furthermore, we regridded these images to the pixel size of 500 μm image ($\sim 14''$). These steps were performed using the convolution kernels available in the HIPE software. Next, the sky background flux level was estimated to be 0.060, 0.133, 0.198, and $-0.095 \text{ Jy pixel}^{-1}$ for the 500, 350, 250, and 160 μm images (size of the selected region $\sim 13'.4 \times 14'.8$; centered at: $l = 183^\circ.181$; $b = -0^\circ.354$), respectively. The negative flux value at 160 μm is obtained due to the arbitrary scaling of the *Herschel* 160 μm image. To avoid diffuse emission linked with the S242 site, the featureless dark field away from the selected target was carefully chosen for the background estimation.

Finally, to generate the temperature and column density maps, a modified blackbody was fitted to the observed fluxes on a pixel-by-pixel basis (see equations 8 and 9 in Mallick et al. 2015). The fitting was performed using the four data points for each pixel, maintaining the dust temperature (T_d) and the column density ($N(\text{H}_2)$) as free parameters. In the analysis, we used a mean molecular weight per hydrogen molecule (μ_{H_2}) of 2.8 (Kauffmann et al. 2008) and an absorption coefficient (κ_ν) of $0.1 (\nu/1000 \text{ GHz})^\beta \text{ cm}^2 \text{ g}^{-1}$, including a gas-to-dust ratio (R_t) of 100, with a dust spectral index (β) of 2 (see Hildebrand 1983). We considered flux uncertainties of the order $\sim 15\%$ in all *Herschel* images, based on the previously reported work by Launhardt et al. (2013). We describe the *Herschel* temperature and column density maps in Section 3.1.1.

2.5. Dust continuum 1.1 mm data

We also obtained Bolocam dust continuum sources at 1.1 mm (v2.1; Ginsburg et al. 2013) from Bolocam Galactic Plane Survey (BGPS). The effective full width at half maximum (FWHM) of the 1.1 mm map (Aguirre et al.

2011) is $\sim 33''$.

2.6. Molecular ^{12}CO line data

To trace the molecular cloud associated with the S242 site, the 2.6 mm ^{12}CO data (beam size $\sim 8'$) were obtained from the 1.2-m CfA telescope (Dame et al. 2001). The line data have a velocity resolution of 0.65 km s^{-1} and a typical rms value of 0.22 K km s^{-1} . One can find more details about the ^{12}CO data in Dame et al. (2001).

2.7. Radio continuum data

We utilized the archival radio continuum data at 1.28 GHz and 1.4 GHz. Radio continuum map at 1.4 GHz (21 cm; beam size $\sim 45''$) was extracted from the NRAO VLA Sky Survey (NVSS; Condon et al. 1998) archive, while the radio continuum data of S242 at 1.28 GHz were retrieved from the GMRT archive³. The GMRT observations were obtained on 30 November 2005 (Project Code: 09SKG01). The GMRT radio data reduction was carried out using the AIPS software, following similar procedures as described in Mallick et al. (2013). The 1.28 GHz map has rms noise of 0.15 mJy/beam and beam size of $\sim 20''.4 \times 20''.4$.

2.8. H I line data

We retrieved 21 cm H I line data from the Canadian Galactic Plane Survey (CGPS; Taylor et al. 2003). The velocity resolution of H I line data is 1.32 km s^{-1} , sampled every 0.82 km s^{-1} . The data have a spatial resolution of $1' \times 1' \text{ csc}\delta$. The line data have a brightness-temperature sensitivity of $\Delta T_B = 3.5 \sin\delta \text{ K}$. One can find more details about the CGPS data in Taylor et al. (2003).

3. RESULTS

3.1. Large-scale physical environment around S242

In this section, we study the distribution of dense materials, molecular gas, and ionized emission toward S242, enabling us to probe the physical environment around the target region.

The study of molecular line data is very essential to trace the physical association of different subregions seen in the large-scale map of a given star-forming region. Based on the CfA ^{12}CO line profile, the molecular cloud linked with the S242 site (hereafter S242 molecular cloud) is traced in a velocity range from -3.25 to 4.55 km s^{-1} (see Figure 1). Figure 1 shows the spatial distribution of the molecular gas in our selected region around S242, revealing an elongated molecular cloud. We have also shown the positions of two IRAS sources (i.e. IRAS 05488+2657 and IRAS 05483+2728) in our selected region. Based on the distribution of molecular emission, we selected a region of $\sim 1^\circ.05 \times 0^\circ.56$ containing the S242 site for our present study, where a majority of molecular gas have been found (see dotted-dashed box in Figure 1). In Figure 2, the integrated ^{12}CO intensity map (see Figure 2a) and the position-velocity maps (see Figures 2b and 2d) are presented. In Figure 2a, we show the CfA ^{12}CO intensity map integrated over -3.25 to 4.55 km s^{-1} . The peak positions of ten dust continuum sources at Bolocam 1.1 mm are also marked in Figure 2a.

Bolocam 1.1 mm dust emission contours are presented in Figure 2c and trace the cold dust. In Figures 2b and 2d, we show galactic position-velocity diagrams of the ^{12}CO emission, indicating the presence of a single velocity component (at peak velocity $\sim 1.5 \text{ km s}^{-1}$) in the direction of our selected target region.

Figure 3a shows a three-color composite map made using the *Herschel* 250 μm in red, *WISE* 22 μm in green, and *WISE* 12 μm in blue. The images at wavelengths longer than 150 μm trace the cold dust emission, while the 12–70 μm emission is sensitive for the warm dust components. Figure 3b shows the *Herschel* sub-mm images overlaid with the NVSS 1.4 GHz continuum emission. The NVSS map allows to infer the spatial distribution of ionized emission which is only found toward the S242 site. In Figures 3a and 3b, an extended filamentary structure (EFS) (extension $\sim 25 \text{ pc}$; average width $\sim 1.3 \text{ pc}$), containing the S242 site, is revealed and is prominently observed in the *Herschel* sub-mm images at 250–500 μm . Note that the Bolocam 1.1 mm dust emission map does not trace the entire EFS as seen in the *Herschel* sub-mm images, however the Bolocam clumps are detected toward the EFS (see Figure 2c). In Figure 1, with the help of the CfA ^{12}CO gas distribution, we find a continuous velocity structure in the direction of S242 and the EFS is embedded within the S242 molecular cloud (see Figures 3a and 3b). In the velocity space, there is only one velocity component observed in the direction of the EFS (see Figures 2b and 2d). This implies the existence of a single EFS. The peak positions of ten dust continuum sources at 1.1 mm are also shown in Figures 3a and 3b and are mainly distributed toward the EFS (also see Section 3.1.1 for quantitative estimate). This particular result gives a hint about fragmentation of the filamentary cloud. To further infer this signature, we estimated virial mass (M_{vir}) and virial parameter ($M_{\text{vir}}/M_{\text{cloud}}$) of the S242 molecular cloud using the observed physical parameters. Using the NANTEN ^{13}CO (1-0) line data (beam size $\sim 2''.7$), Kawamura et al. (1998) reported M_{cloud} ($\sim 7000 M_\odot$), radius ($R_c \sim 7 \text{ pc}$), and line width ($\Delta V = 2.1 \text{ km s}^{-1}$) for the S242 molecular cloud. The virial mass of a cloud of radius R_c (in pc) and line-width ΔV (in km s^{-1}) is defined as $M_{\text{vir}} (M_\odot) = k R_c \Delta V^2$ (MacLaren et al. 1988), where the geometrical parameter, $k = 126$, for a density profile $\rho \propto 1/r^2$. A virial parameter less than 1 indicates the cloud prone to collapse, and greater than 1 is resistant to collapse. In the present case, we obtain $M_{\text{vir}} \sim 3890 M_\odot$, which is less than M_{cloud} . This implies that the virial parameter is less than 1, suggesting the cloud is unstable against gravitational collapse.

In Figures 3a and 3b, we find that the S242 site has a shell-like appearance where noticeable warm dust emission at MIR is seen. In general, the ionized gas and the warm dust emissions are seen systematically correlated within H II regions (e.g. Deharveng et al. 2010). With the knowledge of the presence and absence of the radio continuum emission, we find two distinct ends of the EFS. One EFS end contains the S242 H II region, while the other EFS end is seen without noticeable ionized emission (see Figure 3b). Note that a majority of the dust continuum sources at 1.1 mm are seen at both the ends of the EFS.

³ <https://naps.ncra.tifr.res.in/goa/mt/search/basicSearch>

Together, Figures 1 and 3 allow to probe the S242 molecular cloud, EFS, dust continuum sources at 1.1 mm, and H II region in our selected site probed in this paper.

3.1.1. *Herschel* temperature and column density maps

In this section, the temperature and column density maps derived using the *Herschel* continuum images are discussed. The final temperature and column density maps (resolution $\sim 37''$) are shown in Figures 4a and 4b, respectively.

In the *Herschel* temperature map, the S242 H II region is associated with the considerably warmer gas ($T_d \sim 22$ – 32 K) (see Figure 4a). The map clearly traces the spatial extent of warm dust emission linked with the S242 site, where the ionized emission is observed. The temperature map reveals temperature variations toward the EFS (see areas near both the EFS ends). The EFS is traced in a temperature range of about 10–12 K away from the S242 H II region. In Figures 4b, 5a, and 5b, the EFS (length ~ 25 pc) is evident in the *Herschel* column density map at a contour level of 1.5×10^{21} cm^{-2} and several condensations are also seen toward this feature (also see Figure 5c). The S242 site is located in the highest column density region (peak $N(\text{H}_2) \sim 2.7 \times 10^{22}$ cm^{-2} ; $A_V \sim 29$ mag). Here, we used a relation ($A_V = 1.07 \times 10^{-21} N(\text{H}_2)$; Bohlin et al. 1978) between optical extinction and hydrogen column density. In the column density map (see Figure 5a), the “*clumpfind*” IDL program (Williams et al. 1994) is employed to trace the clumps and to find their total column densities. We used several column density contour levels as an input parameter for the “*clumpfind*” and the lowest contour level was assigned at 3σ . Eighteen clumps are identified in the map and are labeled in Figure 5c. Furthermore, the boundary of each clump is also shown in Figure 5c. Eleven out of eighteen clumps (e.g., 1 to 11) are found toward the EFS. We have also determined the mass of each clump using its total column density. The mass of a single *Herschel* clump is estimated using the following formula:

$$M_{clump} = \mu_{\text{H}_2} m_H \text{Area}_{pix} \Sigma N(\text{H}_2) \quad (1)$$

where μ_{H_2} is assumed to be 2.8, Area_{pix} is the area subtended by one pixel, and $\Sigma N(\text{H}_2)$ is the total column density. The mass of each *Herschel* clump is tabulated in Table 1. The table also lists effective radius, peak column density, peak temperature, and mean central number density (n_c) of each clump. The clump masses vary between $25 M_\odot$ and $1020 M_\odot$. We also find peak temperatures, mean central number densities, and peak column densities (corresponding extinction) of the clumps ranging from 10–26 K, 505–2575 cm^{-3} , and 1.9 – 27×10^{21} cm^{-2} ($A_V = 2$ – 29 mag), respectively. The mean central number density of each clump refers to the average number density along the line of sight and is obtained from the peak column density divided by the size of each clump. Eleven clumps, which are distributed toward the EFS, have masses varying between 150 and $1020 M_\odot$. Interestingly, massive clumps ($M_{clump} \sim 260, 700, 700,$ and $1020 M_\odot$) are spatially seen at both the EFS ends (also see Table 1). The virial mass analysis of these clumps is not performed in this paper, due to non-availability of

optically thin line data (such as, NH_3 and CS).

We have also obtained a total column density inside the contour of $N(\text{H}_2) = 1.5 \times 10^{21}$ cm^{-2} and have computed a total mass of the EFS (M_{EFS}) to be $\sim 5000 M_\odot$. Adopting the value of M_{EFS} and length of EFS (~ 25 pc), the mass per unit length is calculated to be $\sim 200 M_\odot \text{pc}^{-1}$. Note that there is no knowledge of the inclination angle, i , of the EFS, and for reference, we have adopted here $i = 0$. Due to the inclination, the line mass can be affected by a factor of $\cos i$ (e.g., Kainulainen et al. 2016). Hence, the observed mass per unit length value can be considered as an upper limit.

3.2. *Star formation activities in and around S242*

The infrared excess emission displayed by sources is an extremely powerful utility to probe the embedded young stellar populations. In a given star-forming region, the knowledge of spatial distribution of these young stellar populations helps to infer the star formation activities. In this section, we describe the identification and classification schemes of young stellar objects (YSOs) using the GPS-2MASS and GLIMPSE360 photometric data from 1–5 μm . Furthermore, to investigate the young stellar clusters, the distribution of YSOs is also presented in and around S242.

The dereddened color-color space ($[\text{K}-[3.6]]_0$ and $[[3.6]-[4.5]]_0$) is a very promising tool to identify infrared-excess sources (e.g. Gutermuth et al. 2009). We computed the dereddened color-color plot ($[\text{K}-[3.6]]_0$ and $[[3.6]-[4.5]]_0$) using the GLIMPSE360 and 2MASS photometric data at 1–5 μm . The dereddened colors were obtained using the color excess ratios listed in Flaherty et al. (2007). Using the dereddened color conditions presented in Gutermuth et al. (2009), we obtain 192 (39 Class I and 153 Class II) YSOs in our selected region probed in this paper. One can also infer possible dim extragalactic contaminants from the selected YSOs with additional conditions (i.e., $[3.6]_0 < 15$ mag for Class I and $[3.6]_0 < 14.5$ mag for Class II) (e.g., Gutermuth et al. 2009). The dereddened 3.6 μm magnitudes were obtained using the observed color and the reddening laws (from Flaherty et al. 2007). In Figure 6a, we show the $[\text{K}-[3.6]]_0$ versus $[[3.6]-[4.5]]_0$ color-color plot for the sources. The selected Class I and Class II YSOs are highlighted by the red circles and blue triangles, respectively.

We also find some additional YSOs having detections only in the H and K bands using the GPS-2MASS data. Note that the UKIDSS-GPS NIR data have better spatial resolution and are three magnitudes deeper than those of 2MASS data. We employed a color-magnitude (H–K/K) diagram to obtain additional young stellar populations, which are shown in Figure 6b. The diagram allows to depict the red sources having H–K > 1.1 mag. We obtained this color criterion based on the color-magnitude analysis of a nearby control field. In Figure 6b, the selected young stellar populations are highlighted by blue triangles. We identify 101 additional YSOs using the color-magnitude space in our selected region.

Using the GPS-2MASS and GLIMPSE360 data at 1–5 μm , our analysis yields a total of 293 YSOs in our selected region around S242. In Figure 6c, we have overlaid the positions of all the selected YSOs on the *Herschel*

column density map. A majority of these YSOs are distributed toward the filamentary structure. The Class I YSOs are located only in the areas of high column density.

3.3. Clustering of YSOs

In this section, we study the individual groups or clusters of YSOs based on their spatial distribution and the statistical surface density utility. In Figures 7a and 7b, to trace the groups/clusters of YSOs, we have superimposed the surface density contours of YSOs on the *Herschel* column density and temperature maps. The surface density map of YSOs is produced using the nearest-neighbour (NN) technique (e.g., Gutermuth et al. 2009; Bressert et al. 2010; Dewangan et al. 2015). Using a $5''$ grid and 6 NN at a distance of 2.1 kpc, the surface density map of 293 YSOs is computed in a manner similar to that described in Dewangan et al. (2015). The clusters of YSOs are mainly seen at both the EFS ends (see Figures 7a and 7b), however, there is a noticeable presence of young stellar populations toward the EFS without any clustering away from its both the ends (i.e. its center; see Figure 6c). Furthermore, a cluster of YSOs is also evident toward the *Herschel* clumps, nos. 14 and 15, which are spatially distributed away from the EFS (see Figure 7a).

Together, the star formation activities have been found toward the clumps linked with the EFS and other *Herschel* clumps.

3.3.1. S242 H II region

In Figure 8, we present a zoomed-in view of the S242 site using the *Spitzer*-IRAC ratio map and the radio continuum maps. In Figures 8a and 8b, the area around the S242 site is chosen based on the spatial extent of the warm dust emission (see Figure 7b). In combination with the radio continuum map, the *Spitzer*-IRAC ratio map of $4.5 \mu\text{m}/3.6 \mu\text{m}$ emission is used here to infer the signatures of molecular outflows and the impact of a massive star on its surroundings (e.g., Dewangan et al. 2016, 2017). IRAC $3.6 \mu\text{m}$ band harbors polycyclic aromatic hydrocarbon (PAH) emission at $3.3 \mu\text{m}$ as well as a prominent molecular hydrogen feature at $3.234 \mu\text{m}$ ($\nu = 1-0 O(5)$). IRAC $4.5 \mu\text{m}$ band contains a hydrogen recombination line $\text{Br}\alpha$ ($4.05 \mu\text{m}$) and a prominent molecular hydrogen line emission ($\nu = 0-0 S(9)$; $4.693 \mu\text{m}$), which is produced by outflow shocks. It is known that IRAC $3.6 \mu\text{m}$ and $4.5 \mu\text{m}$ images have almost identical point response functions, therefore the ratio of $4.5 \mu\text{m}$ to $3.6 \mu\text{m}$ images can be used to directly produce a ratio map of $4.5 \mu\text{m}/3.6 \mu\text{m}$ emission (see Figure 8) (e.g., Dewangan et al. 2016). In Figure 8a, we infer the bright and dark/black regions in the ratio map of $4.5 \mu\text{m}/3.6 \mu\text{m}$ emission. In ratio $4.5 \mu\text{m}/3.6 \mu\text{m}$ map, the bright emission regions trace the excess of $4.5 \mu\text{m}$ emission, while the black or dark gray regions depict the excess of $3.6 \mu\text{m}$ emission. In Figures 8a and 8b, the ionized emissions at 1.28 and 1.4 GHz are distributed within a shell-like morphology. Due to the presence of $3.3 \mu\text{m}$ PAH feature in the $3.6 \mu\text{m}$ band, the dark/black regions surrounding the ionized emission appear to trace photodissociation regions (or photon-dominated regions, or PDRs). Furthermore, the bright emission regions at one of the ends of the EFS containing the S242 site, where

the radio continuum emission is absent and three clusters of YSOs are found, appear to probably trace the outflow activities (see Figure 8b). This interpretation can be supported by the presence of the CO and H_2 outflow signatures in the embedded clusters near IRAS 05490+268 (e.g., Snell et al. 1990; Varricatt et al. 2010).

In Figure 9a, we present an $\text{H}\alpha$ image overlaid with the NVSS 1.4 GHz emission, showing the spatial match between the radio continuum emission and the $\text{H}\alpha$ emission. The position of a previously characterized B0V star (BD +26 980) appears near the peak of radio continuum emission. The surface density contours of the identified YSOs are also highlighted in Figure 9a. In Figure 9b, we show a three-color composite map made using the *Herschel* $70 \mu\text{m}$ in red, *Spitzer* $4.5 \mu\text{m}$ in green, and IPHAS $\text{H}\alpha$ in blue. The color composite map is superimposed with the GMRT 1.28 GHz emission and positions of two 1.2 mm dust continuum peaks (from Beuther et al. 2002). In order to compare the spatial distribution of dust temperature and column density with the ionized emission, the *Herschel* temperature and column density maps of the S242 site are shown in Figures 9c and 9d, respectively. We find the YSO clusters toward the high column density materials. Additionally, there is a lack of column density material within the S242 H II region. Earlier in Section 3.1.1, we mentioned the spatial correlation between the warm dust emission and the ionized emission (also see Figures 9b and 9c). In Figure 9, one can infer the zoomed-in view of the S242 site, tracing the spatial location of the ionized emission, warm dust emission, high column density material, and the embedded stellar populations.

Using the radio continuum maps, we also compute the Lyman continuum photons and the dynamical age (t_{dyn}) of the S242 H II region. Using the NVSS 1.4 GHz map and the *clumpfind* algorithm, the integrated flux density (S_ν) and the radius (R_{HII}) of the H II region are determined to be 437 mJy and 1.84 pc, respectively. Following the equation given in Matsakis et al. (1976), the number of Lyman continuum photons (N_{uv}) is computed to be $\sim 1.5 \times 10^{47} \text{ s}^{-1}$ ($\log N_{uv} \sim 47.18$) for the S242 H II region (see Dewangan et al. 2016, for more details). In this analysis, we used the integrated flux density value, a distance of 2.1 kpc, and the electron temperature of 10000 K. The value of N_{uv} is found to be consistent with a single ionizing star of spectral type B0.5–B0V (see Table II in Panagia (1973) and also Smith et al. (2002)). The estimate of N_{uv} at GMRT 1.28 GHz frequency also corresponds to a single ionizing star of B0.5–B0V spectral type. These calculations are also in agreement with the previously reported spectral type of the ionizing source of the S242 site (Hunter & Massey 1990).

The equation of the dynamical age of the H II region is given below at a radius R_{HII} (e.g., Dyson & Williams 1980):

$$t_{dyn} = \left(\frac{4 R_s}{7 c_s} \right) \left[\left(\frac{R_{HII}}{R_s} \right)^{7/4} - 1 \right] \quad (2)$$

where c_s is the isothermal sound velocity in the ionized gas ($c_s = 11 \text{ km s}^{-1}$; Bisbas et al. (2009)), R_{HII} is mentioned above, and R_s is the radius of the Strömgen sphere ($= (3 N_{uv}/4\pi n_0^2 \alpha_B)^{1/3}$, where the radiative recombination coefficient $\alpha_B = 2.6 \times 10^{-13} (10^4 \text{ K/T})^{0.7}$

$\text{cm}^3 \text{s}^{-1}$ (Kwan 1997), N_{uv} is mentioned above, and “ n_0 ” is the initial particle number density of the ambient neutral gas). Considering a typical value of n_0 ($=10^3 \text{ cm}^{-3}$), we obtained the dynamical age of the S242 H II region to be ~ 0.5 Myr.

We have also utilized 21 cm H I line data toward the S242 site. Figure 10 shows 21 cm H I velocity channel maps of the S242 site. We find the black or dark gray regions in the H I channel maps which trace the H I self-absorption (HISA) features (e.g., Kerton 2005). In a velocity range of 3.48 to 5.95 km s^{-1} , the shell-like HISA feature is evident in the channel maps. The existence of the HISA features can be explained by the presence of the residual amounts of very cold H I gas in molecular clouds (Burton et al. 1978; Baker & Burton 1979; Burton & Liszt 1981; Liszt et al. 1981; Dewangan et al. 2017).

4. DISCUSSION

The cold dust continuum emission traced in the 160 – $1100 \mu\text{m}$ images has been used to probe the elongated filaments and the distribution of clumps in these filaments (e.g. Schneider et al. 2012; Ragan et al. 2014; Contreras et al. 2016; Li et al. 2016, and references therein). It has been observed that the large-scale filaments are found to be unstable to radial collapse and fragmentation. One of the key questions in star formation research is how the filaments fragment into dense clumps/cores that form star. The gravitational fragmentation process can be employed to explain the presence of “dense clumps/cores” in filaments and can be inferred with a knowledge of the line mass of the filament (M_{line}) (e.g., André et al. 2010). It has been suggested that thermally supercritical filaments are associated with the prestellar clumps/cores and star formation activity, where the mass per unit length greater than the critical value ($M_{\text{line,crit}}$) (i.e., $M_{\text{line}} > M_{\text{line,crit}}$). On the other hand, thermally subcritical filaments ($M_{\text{line}} < M_{\text{line,crit}}$) often lack *Herschel* prestellar clumps/cores and embedded protostars (André et al. 2010). The critical mass per unit length ($M_{\text{line,crit}} = 2c_s^2/G$; where c_s is the isothermal sound speed (i.e. $\sim 0.2 \text{ km s}^{-1}$ at $T = 10 \text{ K}$) and G is the gravitational constant) is needed for a filament to be gravitationally unstable to radial contraction and fragmentation along its length (Inutsuka & Miyama 1997). A critical line mass $M_{\text{line,crit}}$ is equal to $\sim 16 M_\odot/\text{pc} \times (T_{\text{gas}}/10 \text{ K})$ for gas filaments (André et al. 2014), hence one can find $M_{\text{line,crit}} \sim 16 M_\odot/\text{pc}$ at $T = 10 \text{ K}$ (e.g., Ostriker 1964; Kainulainen et al. 2016).

Using the ^{13}CO line data analysis, the elongated S242 molecular cloud is unstable against gravitational collapse. The EFS embedded within the S242 molecular cloud is the most prominent feature observed in the *Herschel* column density map. The *Herschel* temperature map traces ~ 10 – 12 K toward the EFS (except close to the S242 H II region). The observed mass per unit length of EFS is computed to be $\sim 200 M_\odot \text{ pc}^{-1}$, which is much higher than the critical masses per unit length (16 – $48 M_\odot/\text{pc}$) at $T = 10$ – 30 K . For a comparison purpose, André et al. (2016) presented a Table 1 containing the physical parameters of some well-documented filaments ($M_{\text{line}} \sim 4500 M_\odot \text{ pc}^{-1}$ (DR21), $\sim 290 M_\odot \text{ pc}^{-1}$ (Serpens South), $\sim 50 M_\odot \text{ pc}^{-1}$ (Taurus B211/B213), and $\sim 20 M_\odot \text{ pc}^{-1}$ (Musca)). The EFS also contains a chain

of *Herschel* clumps ($M_{\text{clump}} \sim 150$ to $1020 M_\odot$), depicting the evidence of fragmentation along its length. The most massive clumps are seen at both the EFS ends and the S242 H II region is traced at one of the EFS ends. The young stellar populations are also spatially found toward the EFS, indicating a convincing evidence of ongoing star formation activities (see Section 3.2). However, the clusters of YSOs are only observed at both the EFS ends (see Section 3.3). Most recently, Kainulainen et al. (2016) also found the fragmentation strongly at the ends of the Musca cloud. In the long (but finite-sized) filaments, numerical and analytical studies showed that the acceleration of gas is a function of the relative position along the filament and is the greatest at its both the ends (Bastien 1983; Pon et al. 2011, 2012; Clarke & Whitworth 2015, see also Burkert & Hartmann 2004 for a study in a sheet geometry). These higher accelerations indicate shorter local collapse time-scales, suggesting the formation of fragments at the ends of the filament prior to its center (Pon et al. 2011, 2012). Pon et al. (2011) reported that the local collapse may act a factor of two-to-three faster at the ends of the filament than at its center (see Figures 5 and 6 in Pon et al. 2011). Additionally, Heitsch et al. (2008) presented three-dimensional models of molecular cloud formation in large-scale colliding flows including self-gravity, and found that global collapse of a molecular cloud produces centrally located large-scale filaments, while local gravitational collapse can cause massive cores to form far away from the centers of molecular clouds on much shorter timescales than the global dynamical collapse time. Taking into account the existence of YSO clusters and massive clumps at both the EFS ends, the observed results are in agreement with the outcome of a model of the end-dominated collapse caused by the higher accelerations of gas. Presently, we don’t have optically thin line data (such as, NH_3 and CS) for the EFS, hence, the high-resolution molecular line data will be required to further explore the EFS and its velocity structure.

It has been observationally evident that numerous complex processes involved in star formation operate in a given star-forming complex (e.g., Kang et al. 2010; Dewangan et al. 2016). At least three YSO clusters are found at one EFS end and also appear to be found near the edges of the shell-like morphology linked with the S242 H II region (see Figures 7a, 8b, and 9a). Hence, the detection of YSO clusters surrounding the S242 H II region also indicates the applicability of triggered star formation scenario (via an expanding H II region) in the S242 site. The dynamical or expansion age of the H II region is computed to be ~ 0.5 Myr (for $n_0 = 10^3 \text{ cm}^{-3}$) (see Section 3.3.1). The average lifetimes of Class I and Class II YSOs are estimated to be ~ 0.44 Myr and ~ 1 – 3 Myr, respectively (Evans et al. 2009). Considering these typical ages of YSOs and the dynamical age of the S242 H II region, it appears that the S242 H II region is too young to trigger further star formation. Hence, the star formation in the S242 site is unlikely influenced by the S242 H II region.

5. SUMMARY AND CONCLUSIONS

In the present work, we have studied the physical environment, molecular gas distribution, and stellar population in and around the S242 site, using the

multi-wavelength data. We have chosen a field of $\sim 1^\circ.05 \times 0^\circ.56$ containing the sources, S242, IRAS 05490+2658, IRAS 05488+2657, and IRAS 05483+2728. The aim of this study is to investigate the physical environment and star formation processes in and around the selected target. The major results of our multi-wavelength analysis are the following:

- The molecular cloud associated with the S242 site (and three IRAS sources, IRAS 05490+2658, IRAS 05488+2657, and IRAS 05483+2728) is depicted in a velocity range from -3.25 to 4.55 km s^{-1} and has spatially elongated appearance.
- The distribution of ionized emission toward the S242 site detected in the NVSS 1.4 GHz and GMRT 1.28 GHz continuum maps and H α image is almost spherical. The ionizing photon flux value computed at 1.4 GHz corresponds to a single ionizing star of B0.5V–B0V spectral type. The dynamical age of the S242 H II region is computed to be $\sim 0.5 \text{ Myr}$ (for $n_0 = 10^3 \text{ cm}^{-3}$). In the *Herschel* column density map, the S242 site is located in the highest column density region (peak $N(\text{H}_2) \sim 2.7 \times 10^{22} \text{ cm}^{-2}$; $A_V \sim 29 \text{ mag}$).
- An elongated filamentary structure (EFS) is observed in the *Herschel* column density map and is embedded within the S242 molecular cloud. The S242 H II region is located at one of the EFS ends. The highest temperature ($\sim 32 \text{ K}$) is found toward the S242 H II region. In the temperature map, the EFS is depicted in a temperature range of about 10–12 K (except near the S242 H II region). The temperature map traces temperature variations toward the EFS (see areas near both the ends of the EFS).
- The EFS has an observed mass per unit length of $\sim 200 M_\odot \text{ pc}^{-1}$ larger than the critical value of $\sim 16 M_\odot \text{ pc}^{-1}$. Eleven *Herschel* clumps are found toward the EFS and their masses vary between $150 M_\odot$ and $1020 M_\odot$. This implies that the fragmentation has been occurred along the EFS's length. The most massive clumps are observed at both the EFS ends and the S242 H II region is located at one of the EFS ends.
- 293 YSOs are identified in our selected field and a majority of these are spatially traced toward the EFS. The clusters of YSOs are exclusively found at both the EFS ends, revealing the star formation activities.

Taking into account the observational outcomes presented in this paper, the results favour a star formation model of the end-dominated collapse originated by the higher accelerations of gas.

We thank the anonymous reviewer for constructive comments and suggestions. The research work at Physical Research Laboratory is funded by the Department of Space, Government of India. This work is based on data obtained as part of the UKIRT Infrared Deep Sky Survey. This publication made use of data products from the Two Micron All Sky Survey (a joint project of the University of Massachusetts and the Infrared Processing and Analysis Center / California Institute of Technology, funded by NASA and NSF), archival data obtained with the *Spitzer* Space Telescope (operated by the Jet Propulsion Laboratory, California Institute of Technology under a contract with NASA). This paper makes use of data obtained as

part of the INT Photometric H α Survey of the Northern Galactic Plane (IPHAS, www.iphas.org) carried out at the Isaac Newton Telescope (INT). The INT is operated on the island of La Palma by the Isaac Newton Group in the Spanish Observatorio del Roque de los Muchachos of the Instituto de Astrofísica de Canarias. The IPHAS data are processed by the Cambridge Astronomical Survey Unit, at the Institute of Astronomy in Cambridge. RD acknowledges CONACyT(México) for the PhD grant 370405. AL acknowledges the CONACyT(México) grant CB-2012-01-1828-41.

REFERENCES

- Aguirre, J. E., Ginsburg, A. G., Dunham, M. K., et al. 2011, *ApJS*, 192, 4
- André, P., Men'shchikov, A., Bontemps, S., et al. 2010, *A&A*, 518, L102
- André, P., Di Francesco, J., Ward-Thompson, D., et al. 2014, in *Protostars and Planets VI*, ed. H. Beuther et al. (Tucson, AZ: Univ. Arizona Press), 27
- André, P., Revéret, V., Könyves, V., et al. 2016, *A&A*, 592, 54
- Baker, P., L., & Burton, W., B. 1979, *A&AS*, 35, 129
- Bastien, P. 1983, *A&A*, 119, 109
- Beuther, H., Schilke, P., Menten, K. M., et al. 2002, *ApJ*, 566, 945
- Bisbas, T. G., Wunsch, R., Whitworth, A. P., & Hubber, D. A. 2009, *A&A*, 497, 649
- Blitz, L., Fich, M., & Stark, A. A. 1982, *ApJS*, 49, 183
- Bressert, E., Bastian, N., Gutermuth, R., et al. 2010, *MNRAS*, 409, 54
- Bohlin, R. C., Savage, B. D., & Drake, J. F. 1978, *ApJ*, 224, 13233
- Burton, W., B., Liszt, H., S., & Baker, P., L. 1978, *ApJ*, 219, 67
- Burkert, A., & Hartmann, L. 2004, *ApJ*, 616, 288
- Burton, W., B., & Liszt, H., S. 1981, in *Origin of Cosmic Rays*, eds. G. Setti, G. Spada, & A. W. Wolfendale, IAU Symp., 94, 227
- Clarke, S. D., & Whitworth, A. P. 2015, arXiv:1502.07552
- Condon, J. J., Cotton, W. D., Greisen, E. W., et al. 1998, *AJ*, 115, 1693
- Contreras, Y., Garay, G., Rathborne, J. M., & Sanhueza, P. 2016, *MNRAS*, 456, 2041
- Dame, T. M., Hartmann, Dap, & Thaddeus, P. 2001, *ApJ*, 547, 792
- Deharveng, L., Schuller, F., Anderson, L. D., et al. 2010, *A&A*, 523, 6
- Dewangan, L. K., Luna, A., Ojha, D. K., et al. 2015, *ApJ*, 811, 79
- Dewangan, L. K., Ojha, D. K., Luna, A., et al. 2016, *ApJ*, 819, 66
- Dewangan, L. K., Ojha, D. K., Zinchenko, I., Janardhan, P., & Luna, A. 2017, *ApJ*, 834, 22
- Drew, J. E., Greimel, R., Irwin, M.J., et al. 2005, *MNRAS*, 362, 753
- Dyson, J. E., & Williams, D. A. 1980, *Physics of the Interstellar Medium* (New York: Halsted Press)
- Evans, N. J., II, Dunham, M. M., Jørgensen, J. K., et al. 2009, *ApJS*, 181, 321
- Fich, M., Dahl, G. P., & Treffers, R. R. 1990, *AJ*, 99, 622
- Flaherty, K. M., Pipher, J. L., Megeath, S. T., et al. 2007, *ApJ*, 663, 1069
- Ginsburg, A., Glenn, J., Rosolowsky, E., et al. 2013, *ApJS*, 208, 14
- Griffin, M. J., Abergel, A., Abreu, A., et al. 2010, *A&A*, 518L, 3
- Gutermuth, R. A., Megeath, S. T., Myers, P. C., et al. 2009, *ApJS*, 184, 18
- Heitsch, F., Hartmann, L. W., Slyz, A. D., Devriendt, J. E.G., & Burkert, A. 2008, *ApJ*, 674, 316
- Hildebrand, R. H. 1983, *QJRAS*, 24, 267
- Hunter, D. A., & Massey, P. 1990, *AJ*, 99, 846
- Inutsuka, S. & Miyama, S. M. 1997, *ApJ*, 480, 681
- Kainulainen, J., Hacar, A., Alves, J., et al. 2016, *A&A*, 586, 27
- Kawamura, A., Onishi, T., Yonekura, Y. 1998, *ApJS*, 117, 387
- Kauffmann, J., Bertoldi, F., Bourke, T. L., Evans, II, N. J., & Lee, C. W. 2008, *ApJ*, 487, 993
- Kang, M., Bieging, J. H., Kulesa, C. A. et al. 2010, *ApJS*, 190, 58
- Kerton, C. R. 2005, *ApJ*, 623, 235
- Kwan, J. 1997, *ApJ*, 489, 284
- Launhardt, R., Stutz, A. M., Schmiedeke, A., et al. 2013, *A&A*, 551, 98
- Lawrence, A., Warren, S. J., Almaini, O., et al. 2007, *MNRAS*, 379, 1599
- Li, Guang-Xing, Urquhart, J. S., Leurini, S., et al. 2016, *A&A*, 591, 5
- Liszt, H., S., Burton, W., B., & Bania, T., M. 1981, *ApJ*, 246, 74
- MacLaren, I., Richardson, K. M., & Wolfendale, A. W. 1988, *ApJ*, 333, 821
- Mallick, K. K., Kumar, M. S. N., Ojha, D. K., et al. 2013, *ApJ*, 779, 113
- Mallick, K. K., Ojha, D. K., Tamura, M., et al. 2015, *MNRAS*, 447, 2307
- Myers, P. C. 2009, *ApJ*, 700, 1609
- Matsakis, D. N., Evans, N. J., II, Sato, T., & Zuckerman, B. 1976, *AJ*, 81, 172
- Nakamura, F., Sugitani, K., Tanaka, T., et al. 2014, *ApJL*, 791, L23
- Ostriker, J. 1964, *ApJ*, 140, 1056
- Ott, S. 2010, in *Astronomical Society of the Pacific Conference Series*, Vol. 434, *Astronomical Data Analysis Software and Systems XIX*, ed. Y. Mizumoto, K.-I. Morita, & M. Ohishi, 139
- Panagia, N. 1973, *AJ*, 78, 929
- Poglitsch, A., Waelkens, C., Geis, N., et al. 2010, *A&A*, 518L, 2
- Pon, A., Johnstone, D., & Heitsch, F. 2011, *ApJ*, 740, 88
- Pon, A., Toalá, J. A., Johnstone, D., et al. 2012, *ApJ*, 756, 145
- Ragan, S. E., Henning, Th., Tackenberg, J., et al. 2014, *A&A*, 568, 73
- Schneider, N., Csengeri, T., Hennemann, M., et al. 2012, *A&A*, 540, L11
- Skrutskie, M. F., Cutri, R. M., Stiening, R., et al. 2006, *AJ*, 131, 1163
- Smith, L. J., Norris, R. P. F., & Crowther, P. A. 2002, *MNRAS*, 337, 1309
- Snell, R. L., Dickman, R. L., & Huang, Y. L. 1990, *ApJ*, 352, 139
- Tan, J. C., Beltrán, M. T., Caselli, P., et al. 2014, in *Protostars and Planets VI*, ed. H. Beuther et al. (Tucson, AZ: Univ. Arizona Press), 149
- Taylor, A., R., Gibson, S., J., Peracaula, M., et al. 2003, *AJ*, 125, 3145
- Varricatt, W. P., Davis, C. J., Ramsay, S., & Todd, S. P. 2010, *MNRAS*, 404, 661
- Whitney, B., Benjamin, R., Meade, M., et al. 2011, *BAAS*, 43, 241.16
- Williams, J. P., de Geus, E. J., & Blitz, L. 1994, *ApJ*, 428, 693
- Wright, E. L., Eisenhardt, P. R. M., Mainzer, A. K., et al. 2010, *AJ*, 140, 1868

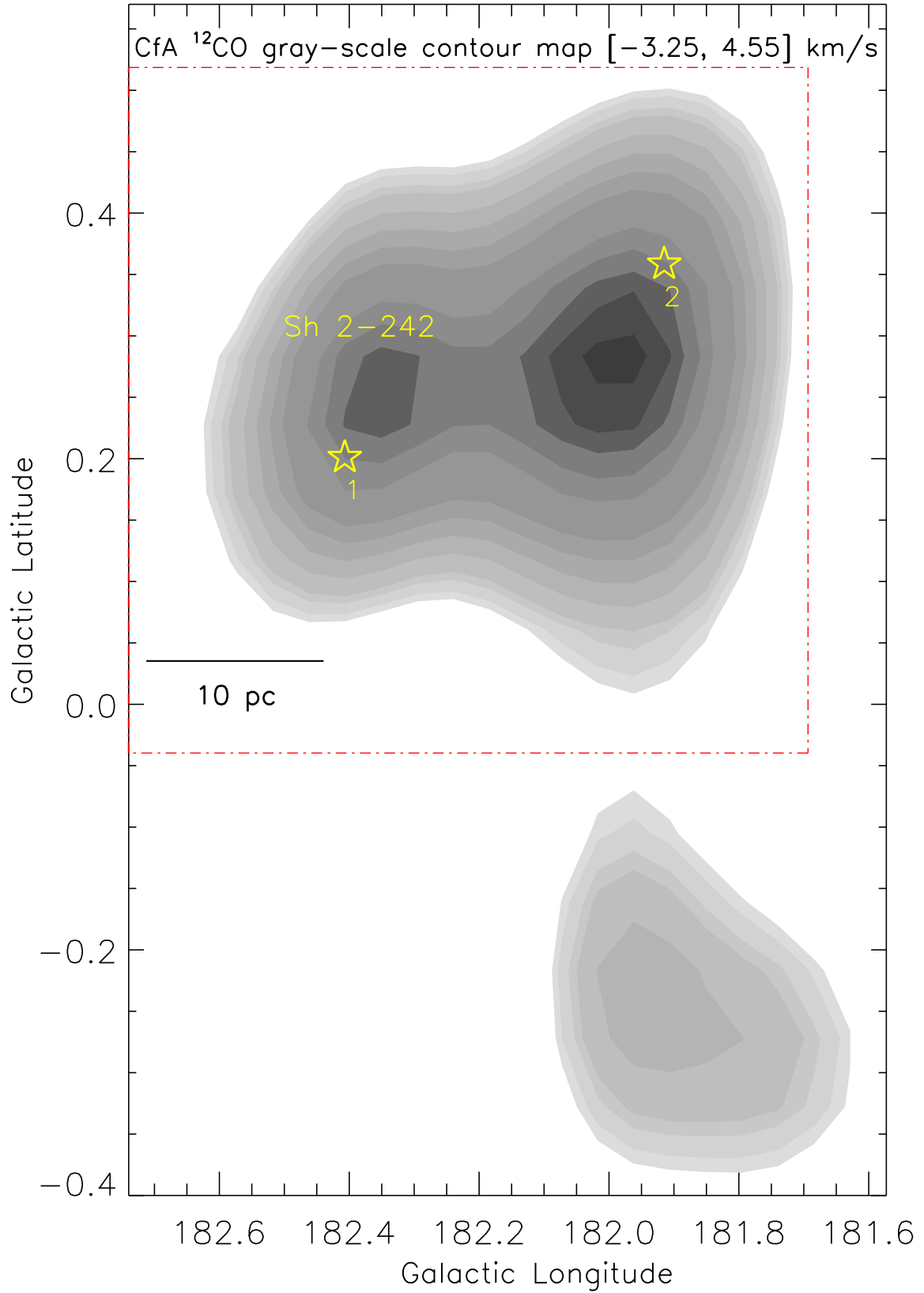


Figure 1. The distribution of molecular gas in the direction of our selected field reveals an elongated molecular cloud. The S242 molecular cloud is depicted in a velocity range from -3.25 to 4.55 km s^{-1} and is shown by a gray-scale contour map. The ^{12}CO emission contours are shown with levels of 43, 45, 48, 50, 55, 60, 65, 70, 80, 85, 90, 94, and 98% of the peak value (i.e., 10.478 K km s^{-1}). The positions of two IRAS sources (IRAS 05488+2657 (#1) and IRAS 05483+2728 (#2)) are also marked by stars. The scale bar corresponding to 10 pc (at a distance of 2.1 kpc) is shown in the left corner. The dotted-dashed red box encompasses the area shown in Figures 2, 3a and 3b. The map is smoothed with a Gaussian function with radius of three.

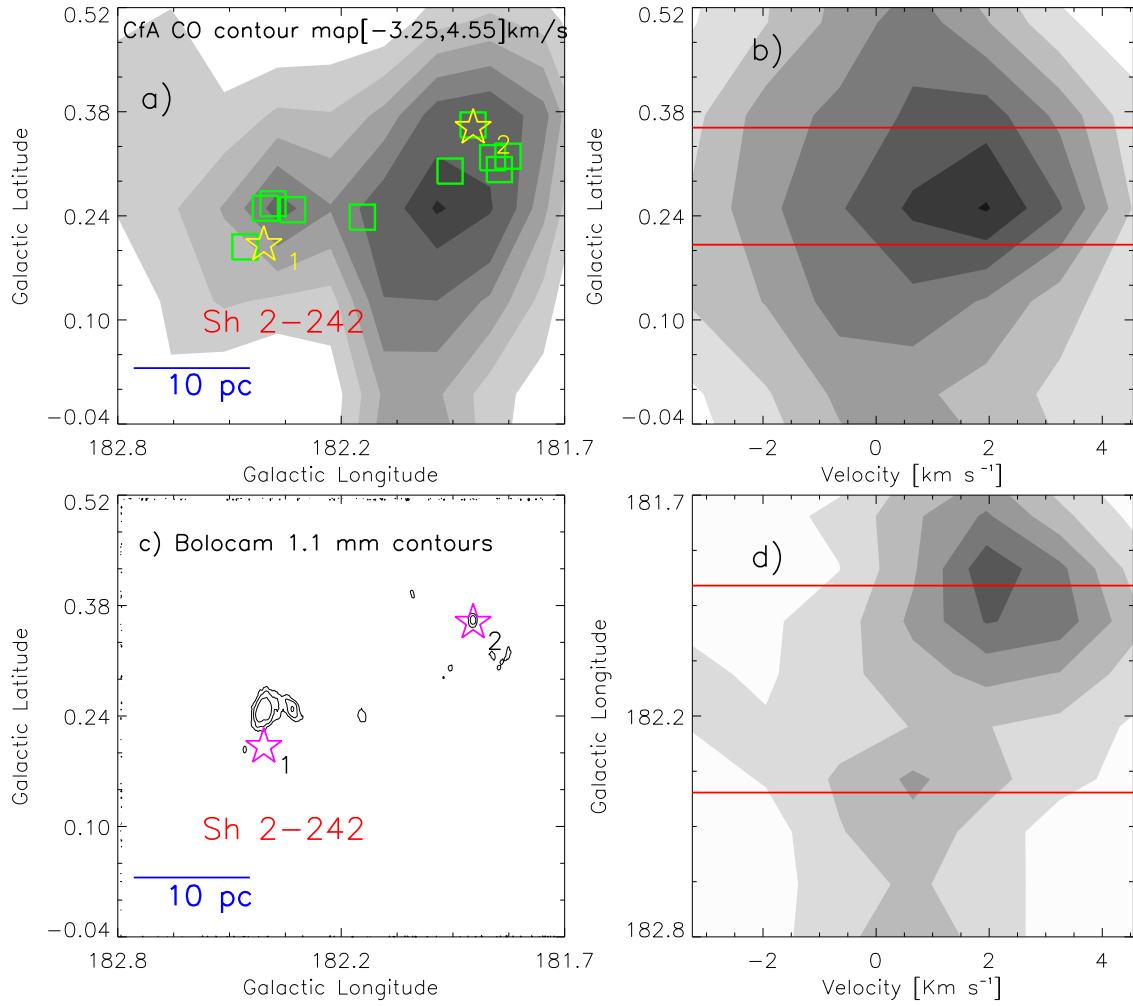


Figure 2. a) Integrated intensity map of CfA ^{12}CO ($J = 1-0$) around S242. The ^{12}CO emission is shown from -3.25 to 4.55 km s^{-1} and is similar to those shown in Figure 1. The positions of dust clumps at 1.1 mm are also marked by square symbols and other marked symbols are similar to those shown in Figure 1. b) Latitude-velocity distribution of ^{12}CO . The ^{12}CO emission is integrated over the longitude from $181^\circ.7$ to $182^\circ.75$. c) Bolocam 1.1 mm dust emission contours are shown with levels of 0.15 , 0.3 , and 0.6 Jy/beam . The other marked symbols are similar to those shown in Figure 1. d) Longitude-velocity distribution of ^{12}CO . The ^{12}CO emission is integrated over the latitude from $-0^\circ.04$ to $0^\circ.52$. In the right panels (i.e., position-velocity maps), two solid red lines show the positions of two IRAS sources (IRAS 05488+2657 (#1) and IRAS 05483+2728 (#2)).

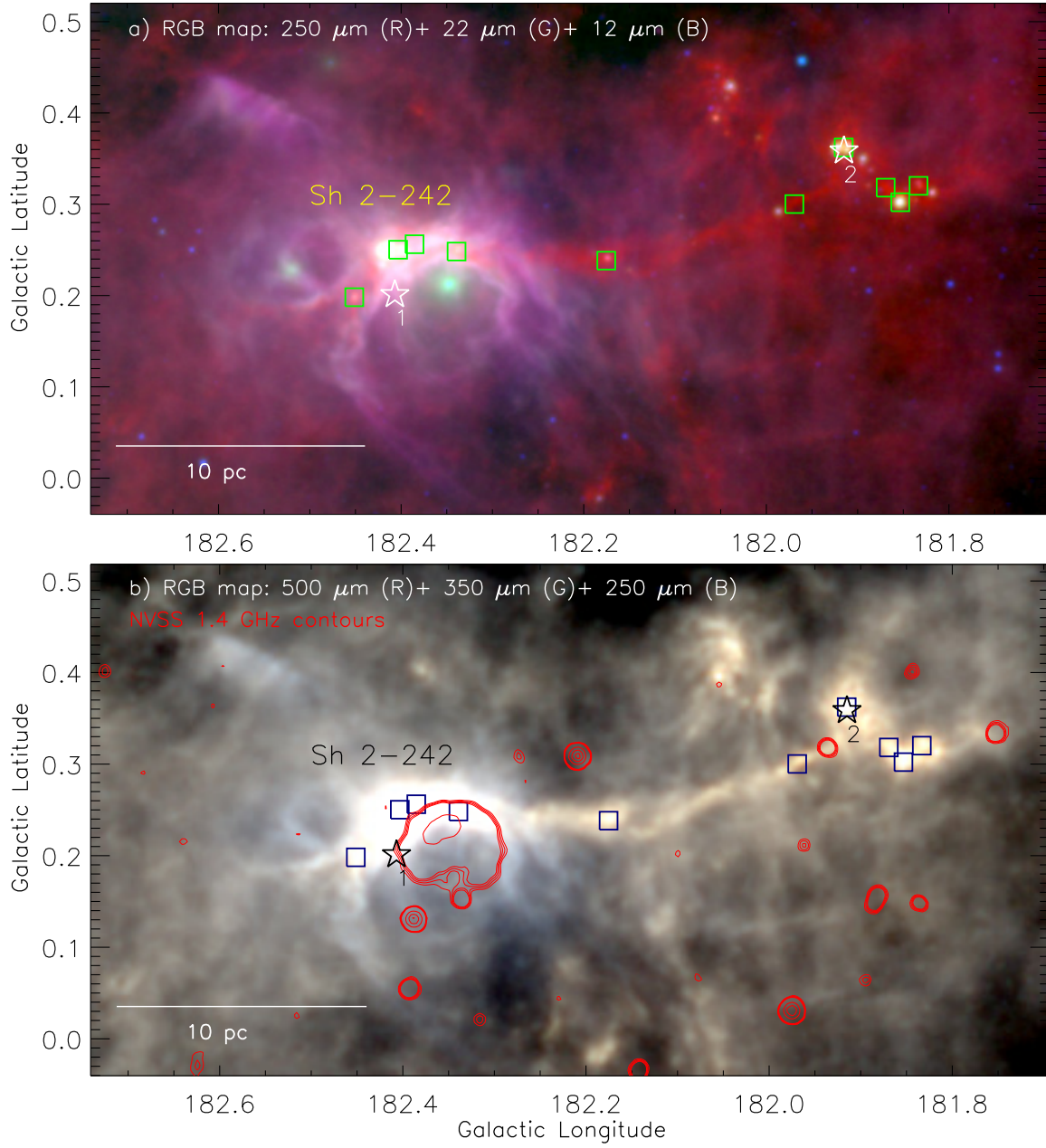


Figure 3. A large scale view of the region around S242 (size of the selected region $\sim 1^\circ.05 \times 0^\circ.56$ ($\sim 38.5 \text{ pc} \times 20.5 \text{ pc}$ at a distance of 2.1 kpc); centered at $l = 182^\circ.217$; $b = 0^\circ.239$). a) Color composite map is the result of the combination of three bands (in logarithmic scale): 250 μm in red (*Herschel*), 22 μm in green (*WISE*), and 12 μm in blue (*WISE*). b) The distribution of the sub-mm emission toward the region around S242. Color composite map is the result of the combination of three *Herschel* bands (500 μm (red), 350 μm (green), and 250 μm (blue)) and is overlaid with the NVSS 1.4 GHz contours. The 1.4 GHz contours (in red) are superimposed with levels of 0.55, 1, 2, 3, 4, 5, 6, 30, 60, and 90% of the peak value (i.e. 0.377 Jy/beam). In both the panels, the positions of dust clumps at 1.1 mm are marked by square symbols and other marked symbols are similar to those shown in Figure 1.

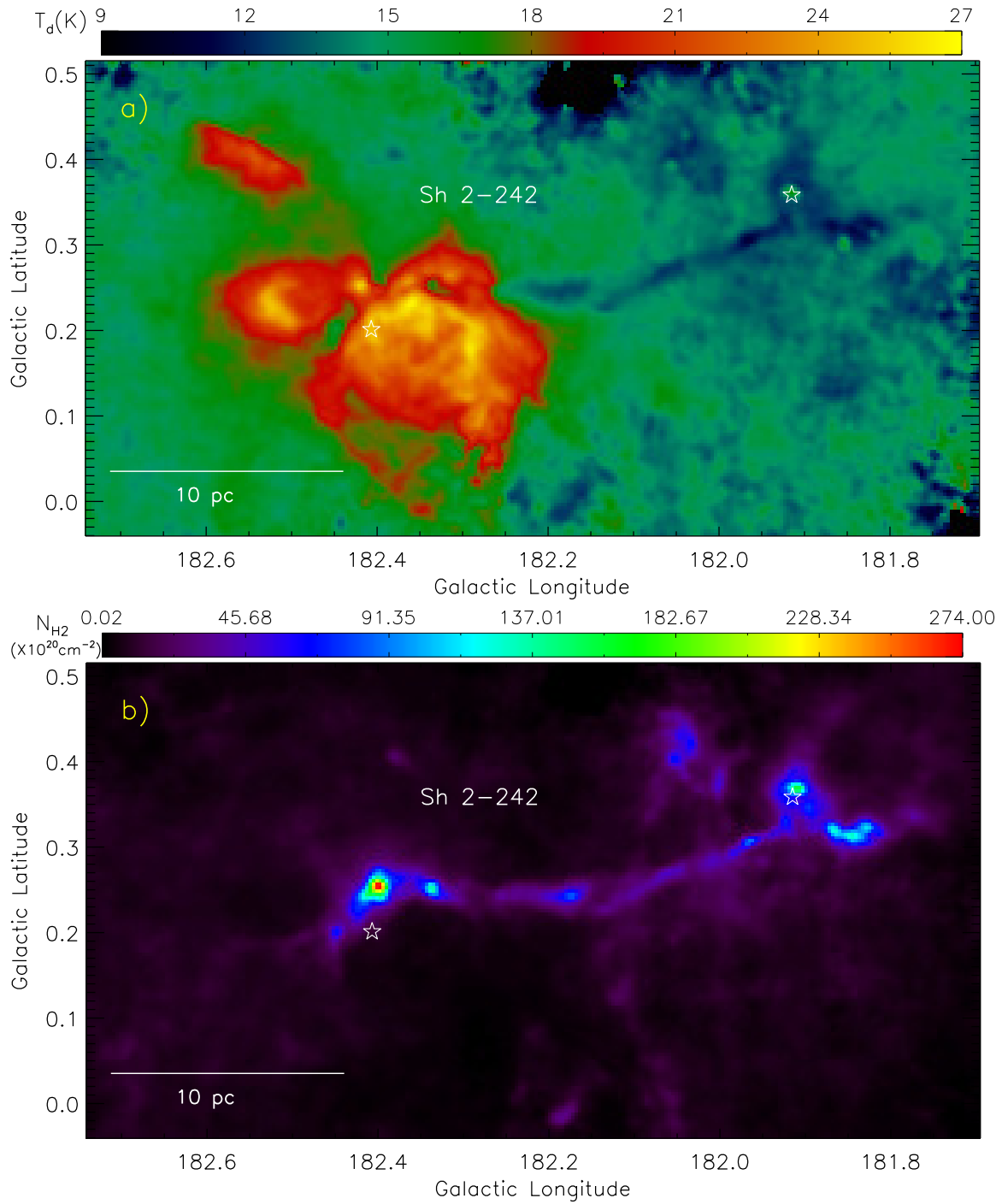


Figure 4. a) *Herschel* temperature map of the region around S242 (see text for details). b) *Herschel* column density ($N(\text{H}_2)$) map of the region around S242 (see text for details). The column density map can be used to infer the extinction using the relation $A_V = 1.07 \times 10^{-21} N(\text{H}_2)$ (Bohlin et al. 1978) and to identify the clumps (see text for details). In both the panels, other marked symbols and labels are similar to those shown in Figure 1.

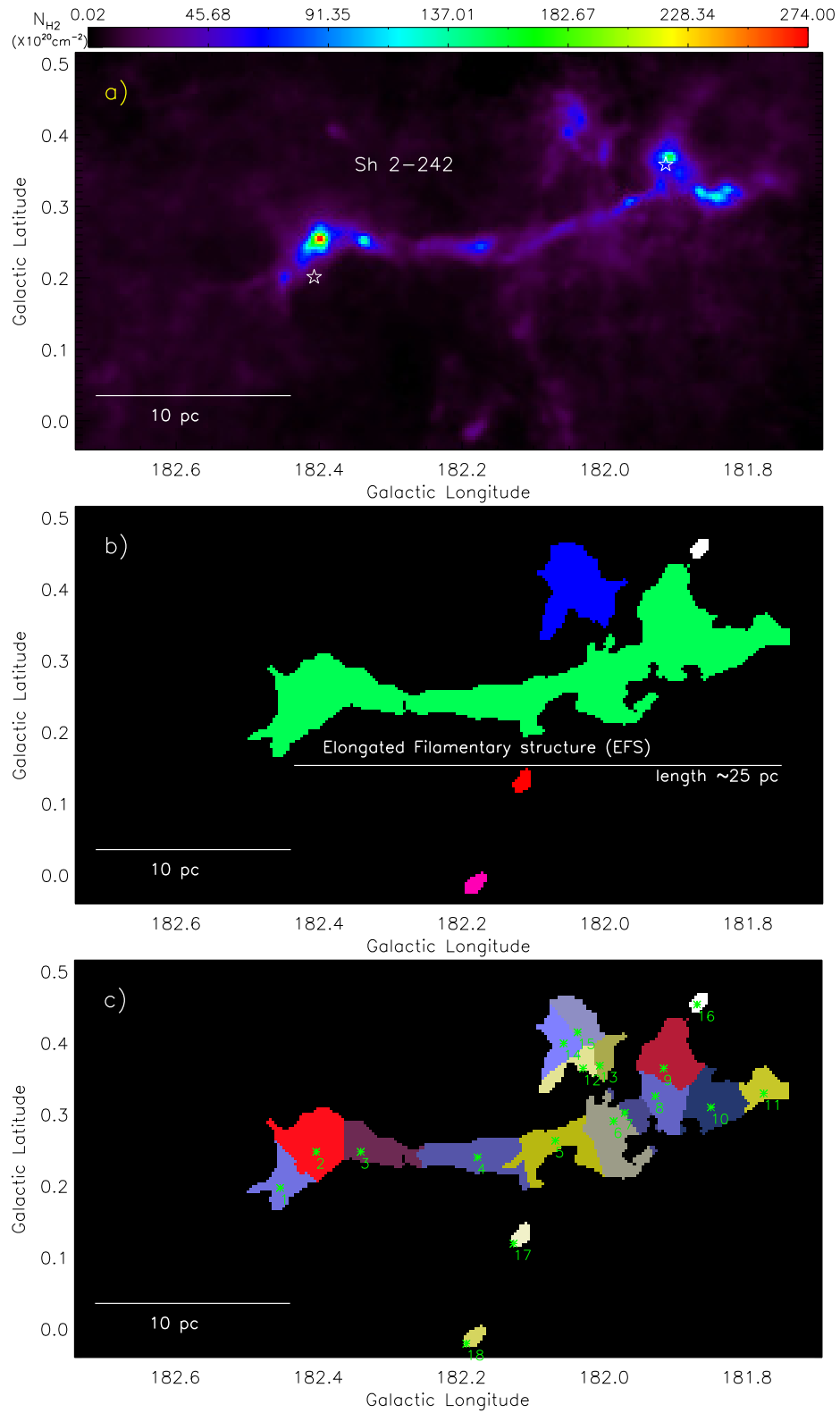


Figure 5. a) *Herschel* column density ($N(\text{H}_2)$) map of the region around S242. b) An elongated filamentary structure (EFS) is traced in the column density map at a contour level of $1.5 \times 10^{21} \text{ cm}^{-2}$. c) The identified clumps are highlighted by asterisks and the boundary of each *Herschel* clump is also shown in figure. The boundary of each *Herschel* clump is highlighted along with its corresponding clump ID.

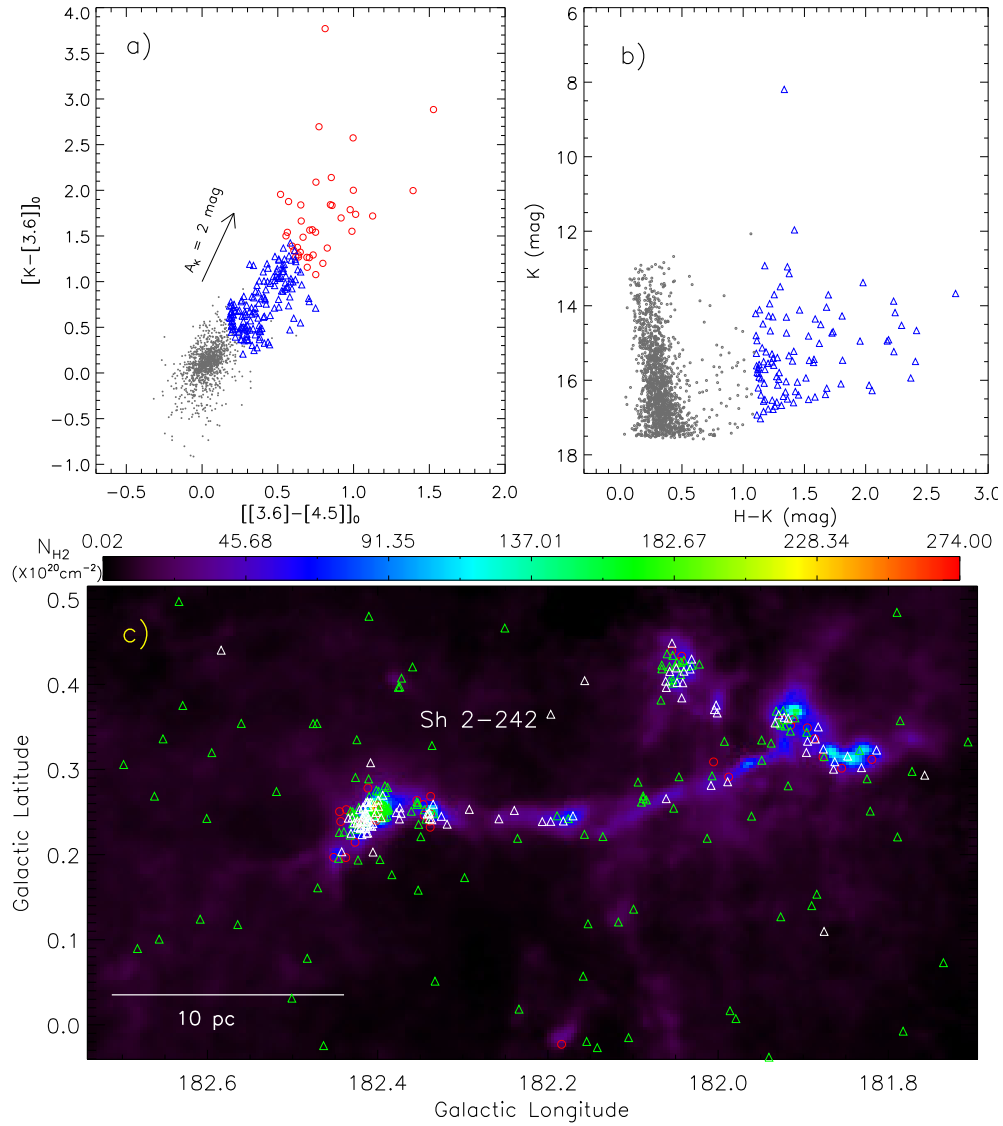


Figure 6. The identification of young stellar populations within the region around S242 (see Figure 3a). a) The dereddened $[K-[3.6]]_0$ vs $[[3.6]-[4.5]]_0$ color-color diagram using the H, K, $3.6 \mu\text{m}$, and $4.5 \mu\text{m}$ data (see text for details). The extinction vector is shown using the average extinction laws from Flaherty et al. (2007). b) Color-magnitude diagram ($H-K/K$) of the sources detected only in H and K bands that have no counterparts in our selected GLIMPSE360 catalog. In each panel, Class I and Class II YSOs are marked by red circles and open blue triangles, respectively, while the dots (in gray) refer the stars with only photospheric emissions. In the color-color diagram, we have shown only 1101 out of 8257 stars with photospheric emissions. In the color-magnitude diagram, we have shown only 1501 out of 20998 stars with photospheric emissions. Due to large numbers of stars with photospheric emissions, we have randomly shown only some of these stars in the diagrams. The positions of all the identified YSOs are shown in Figure 6c. c) The spatial distribution of selected YSOs within the region around S242. The positions of YSOs are overlaid on the *Herschel* column density map. The background map is similar to the one shown in Figure 5a. The positions of Class I and Class II YSOs are shown by circles and triangles, respectively. The YSOs selected using the H, K, $3.6 \mu\text{m}$, and $4.5 \mu\text{m}$ data (see Figure 6a) are shown by red circles and green triangles, whereas the white triangles represent the YSOs identified using the H and K bands (see Figure 6b).

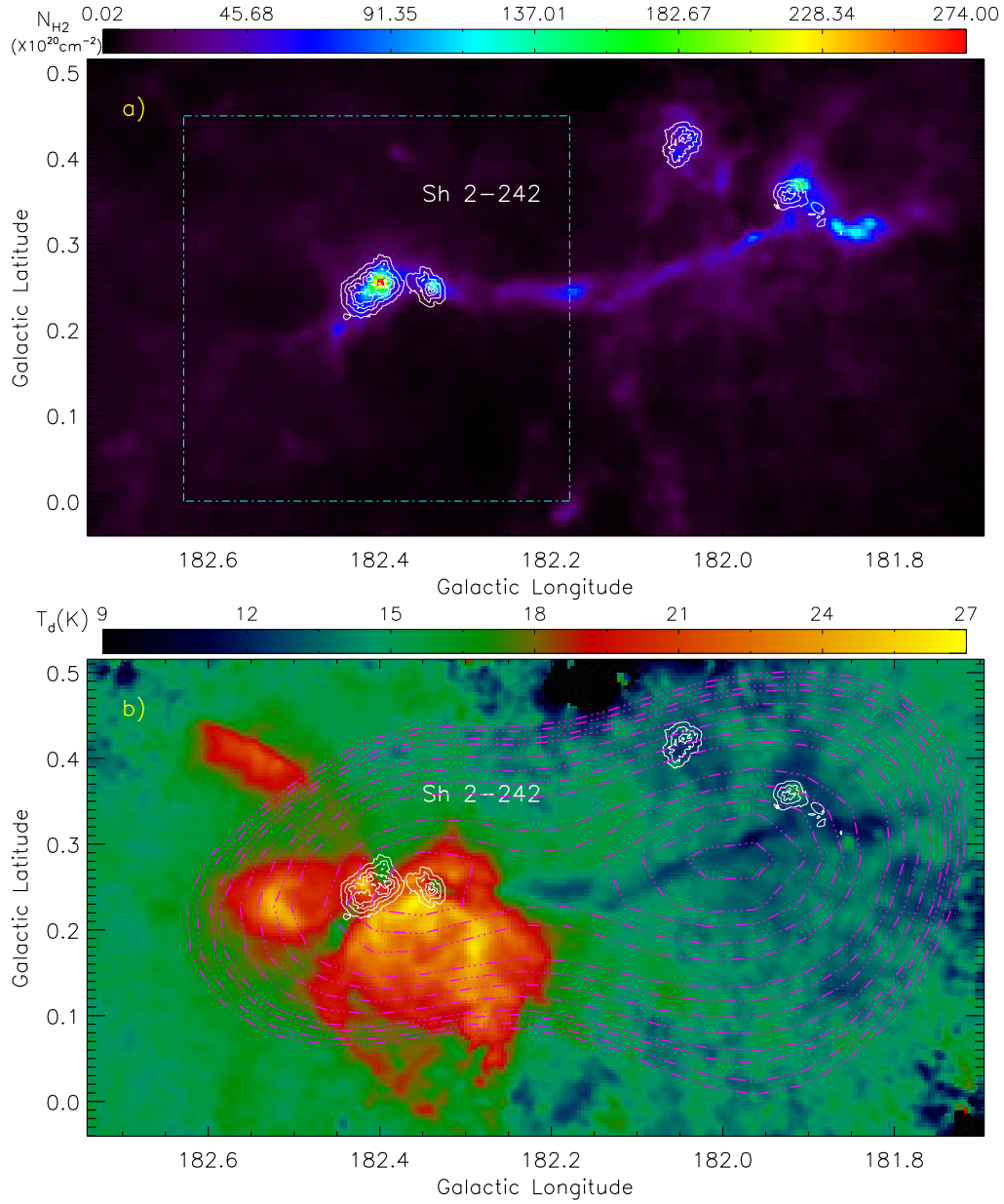


Figure 7. a) The *Herschel* column density map is overlaid with the surface density contours (in white) of the identified YSOs toward the EFS containing the S242 site. The contours are shown at 5, 10, 20, and 40 YSOs/ pc^2 , from the outer to the inner side. The dotted-dashed cyan box encompasses the area shown in Figures 8a and 8b. b) The *Herschel* temperature map is overlaid with the surface density contours (in white) of the identified YSOs toward the EFS containing the S242 site. The ^{12}CO emission contours (dotted-dashed magenta) are also superimposed with levels of 43, 45, 48, 50, 55, 60, 65, 70, 80, 85, 90, 94, and 98 % of the peak value (i.e., $10.478 \text{ K km s}^{-1}$). The integrated ^{12}CO intensity map reveals a continuous velocity structure in the direction of S242. The ^{12}CO map is smoothed with a Gaussian function with radius of three.

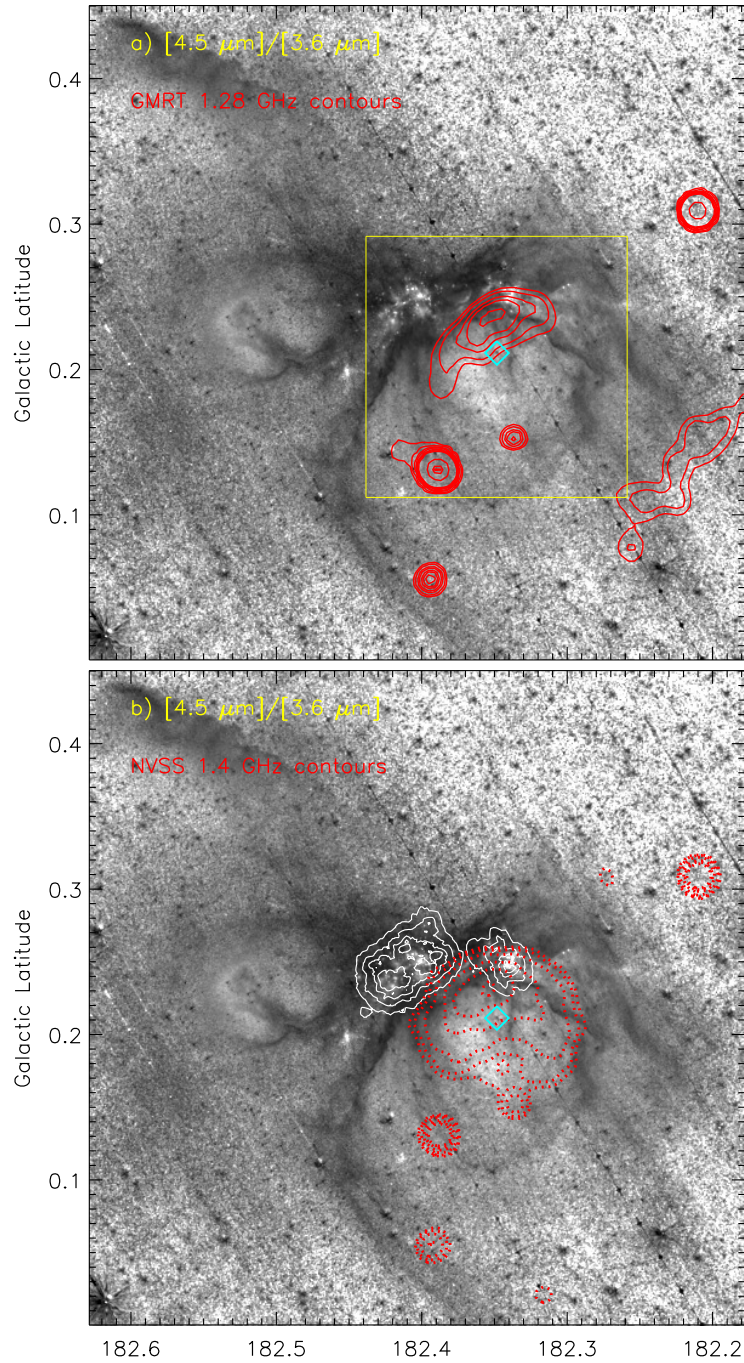


Figure 8. a) *Spitzer* ratio map of 4.5 $\mu\text{m}/3.6 \mu\text{m}$ emission is superimposed with the GMRT radio continuum emission at 1.28 GHz (beam size $\sim 20''.4 \times 20''.4$). The radio contours are shown with levels of 5, 7, 10, 12, 15, 17, 20, 60, 90, and 98% of the peak value (i.e. 13.790 mJy/beam). The solid yellow box encompasses the area shown in Figures 9a, 9b, 9c, 9d, and 10. b) *Spitzer* ratio map of 4.5 $\mu\text{m}/3.6 \mu\text{m}$ emission is overlaid with the NVSS radio continuum emission at 1.4 GHz. The NVSS 1.4 GHz dotted contours (in red) are shown with levels of 3.5, 5.5, 10, 20, 30, and 40% of the peak value (i.e. 0.377 Jy/beam). Figure also shows the surface density contours (in white) of the identified YSOs. The contours are shown at 5, 10, 20, and 40 YSOs/pc², from the outer to the inner side. In each panel, a diamond symbol (in cyan) indicates the location of a massive star, BD+26 980. In both the panels, the ratio map is subjected to median filtering with a width of 4 pixels and smoothed by 4 pixel \times 4 pixel using a boxcar algorithm.

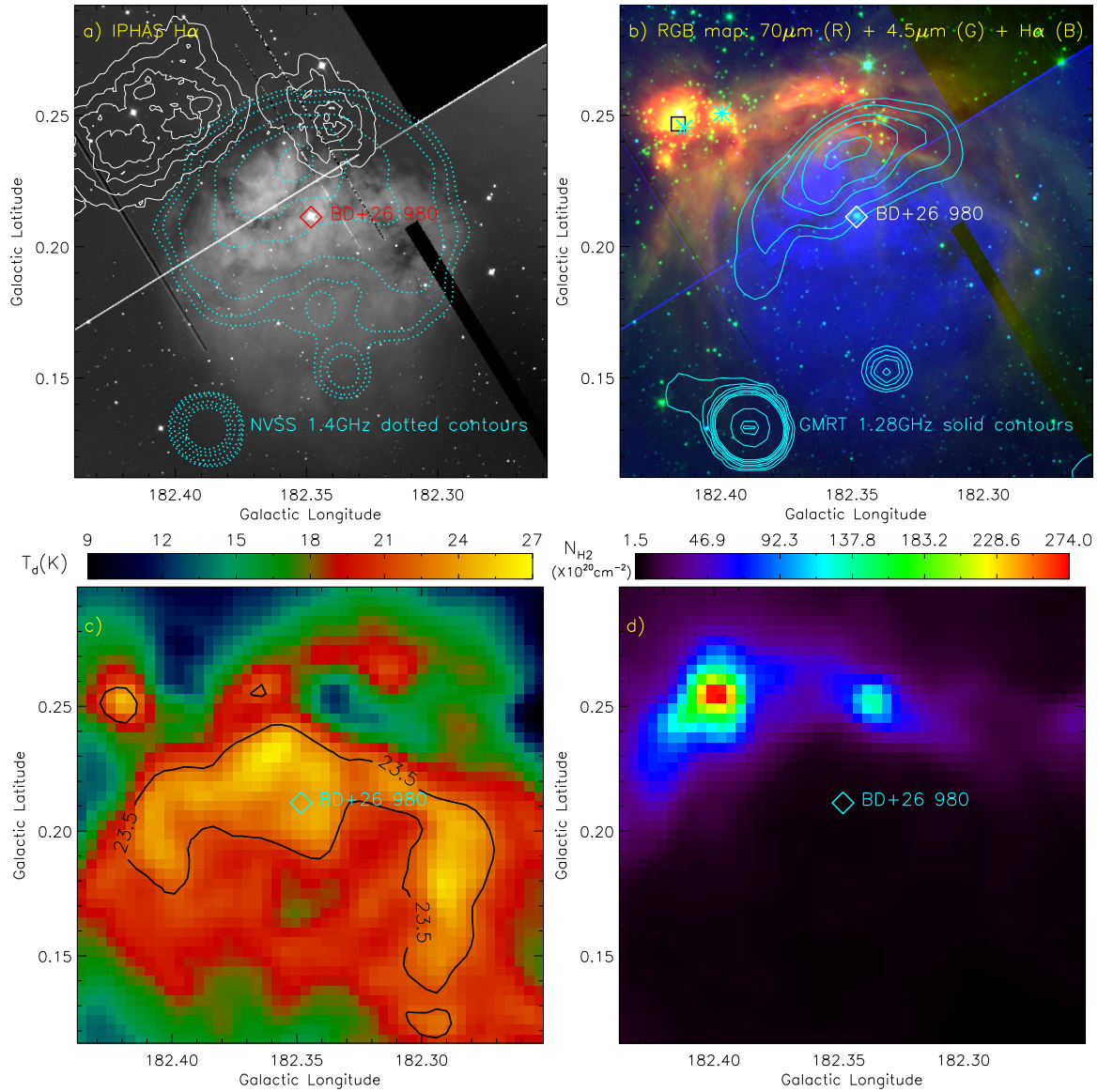


Figure 9. Zoomed-in view of the S242 site. a) The IPHAS H α gray-scale image is superimposed with the NVSS 1.4 GHz contours. The NVSS 1.4 GHz dotted contours (in cyan) are shown with levels of 4, 6, 10, 20, 30, and 40% of the peak value (i.e. 0.377 Jy/beam). Figure also shows the surface density contours (in white) of the identified YSOs. The contours are shown at 5, 10, 20, and 40 YSOs/pc², from the outer to the inner side. b) Color composite map is the result of the combination of 70 μ m (red), 4.5 μ m (green), and H α (blue) and is superimposed with the GMRT 1.28 GHz contours. A square indicates the location of IRAS 05490+2658. Asterisk symbols (in cyan) represent the locations of two 1.2 mm dust continuum peaks (from Beuther et al. 2002). c) *Herschel* temperature map of the S242 site is shown with a temperature contour level of 23.5 K. d) *Herschel* column density map of the S242 site. In all the panels, a diamond symbol indicates the location of BD+26 980.

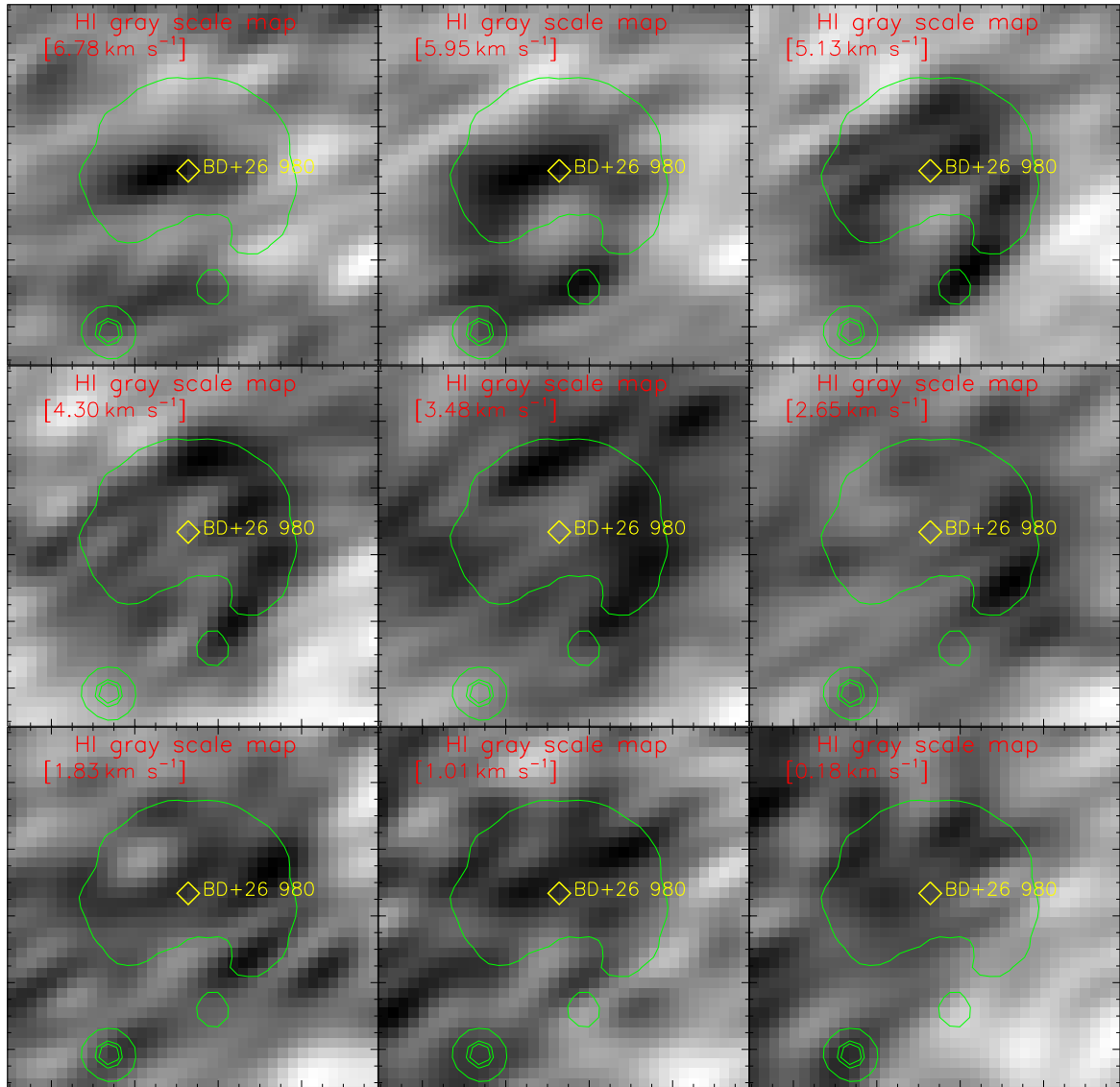


Figure 10. The CGPS 21 cm HI velocity channel maps of the S242 site. The velocity value (in km s^{-1}) is labeled in each panel. In each panel, the NVSS 1.4 GHz contours (in green) are superimposed with levels of 8, 55, and 70% of the peak value (i.e., 0.377 Jy/beam), tracing the ionized hydrogen emission. The location of a massive star BD+26 980 is also marked in the maps. The sphere-like shell morphology of the S242 site is depicted as HI self-absorption features (i.e., cold HI observed in absorption against warmer background HI; Kerton 2005).

Table 1

Physical parameters of the *Herschel* clumps identified in the region around S242 (see Figures 5a and 5c). Column 1 gives the IDs assigned to the clump. Table also lists positions, deconvolved effective radius (R_c), clump mass (M_{clump}), peak column density ($N(\text{H}_2)$), peak temperature (T_d), and mean central number density ($n_c = \text{peak } N(\text{H}_2)/(2 R_c)$). The column density value can also be used to obtain the extinction using the relation $A_V = 1.07 \times 10^{-21} N(\text{H}_2)$. The clump IDs 1–11 are distributed toward the EFS containing the S242 site (see Figure 5c).

ID	l [degree]	b [degree]	R_c (pc)	M_{clump} (M_\odot)	peak $N(\text{H}_2)$ $\times 10^{21}$ (cm^{-2})	peak T_d (K)	n_c (cm^{-3})
1 ^a	182.453	0.197	1.2	260	6.9	16	930
2 ^a	182.403	0.247	1.7	1020	27	26	2575
3	182.341	0.247	1.4	420	13	18	1505
4	182.177	0.239	1.6	480	8.3	14	840
5	182.068	0.263	1.5	380	4.7	14	505
6	181.987	0.290	1.6	405	5.6	13	565
7	181.971	0.302	0.8	150	9	13	1820
8	181.928	0.325	1.2	350	7.2	13	970
9 ^a	181.917	0.364	1.5	700	15.8	16	1705
10 ^a	181.851	0.309	1.5	700	12.7	16	1370
11	181.777	0.329	1.0	150	3.6	13	580
12	182.030	0.364	0.9	100	2.8	12	505
13	182.006	0.368	0.8	125	5.1	16	1030
14	182.057	0.399	1.1	250	6.8	10	1000
15	182.037	0.414	1.1	265	6.7	10	985
16	181.870	0.453	0.5	25	1.9	18	615
17	182.127	0.119	0.5	35	2.1	17	680
18	182.193	-0.021	0.5	45	3.3	15	1070

^a It is found at the EFS end.